Investigating the cause of crossover from charge/spin-stripe insulator to correlated metallic phase in layered T' nickelates $R_4Ni_3O_8$ (R = La, Pr, or Nd)

Dibyata Rout,[1] Sanchayeta Ranajit Mudi,[1] Suman Karmakar,[2] Rajeev Rawat,[2] and Surjeet Singh[1,*]
[1]*Department of Physics, Indian Institute of Science Education and Research, Pune, Maharashtra 411008, India*
[2]*UGC-DAE Consortium for Scientific Research, University Campus, Khandwa Road, Indore 452001, India*

(Received 16 November 2023; accepted 7 August 2024; published 9 September 2024)

The infinite layered (T') nickelates have recently garnered significant attention due to the discovery of superconductivity in hole-doped RNiO$_2$ (R = La, Pr, or Nd), which is the $n = \infty$ member of the series $R_{n+1}Ni_nO_{2n+2}$. Here, we investigate the $n = 3$ member, namely $R_4Ni_3O_8$ (R = La, Pr, or Nd), of this family. The compound $La_4Ni_3O_8$ exhibits simultaneous charge/spin-stripe ordering at $T_N^* = 105$ K, which occurs concomitantly with the onset of the metal-to-insulator (MIT) transition below T_N^*. We investigate the conspicuous absence of this transition in the Pr and Nd analogs of $La_4Ni_3O_8$. For this purpose, we synthesized solid solutions of the form (La, Pr)$_4Ni_3O_8$ and (La, Nd)$_4Ni_3O_8$, and examined the behavior of T_N^* as a function of the average R-site ionic radius ($r_{\bar{R}}$). We show that after an initial quasilinear decrease with decreasing $r_{\bar{R}}$, T_N^* suddenly vanishes in the narrow range $1.134 \leqslant r_{\bar{R}} \leqslant 1.143$ Å. In the same range, we observed the emergence of a weak anomaly in the specific heat, whose onset temperature (T^*) increases as $r_{\bar{R}}$ further decreases reaching a maximum of 13 K for $Nd_4Ni_3O_8$. We suggest, therefore, that the sudden vanishing of charge/spin-stripe/MIT ordering upon decreasing $r_{\bar{R}}$ is related to the appearance of this new electronic phase for $r_{\bar{R}} < r_c$. The nature of this phase or the weak anomaly and the point $r_{\bar{R}} \approx r_c$, where T_N^* vanishes and T^* appears, should be investigated further. In this regard, $Pr_4Ni_3O_8$ and Pr-rich samples should be useful due to the weak magnetization response associated with the Pr sublattice, as shown here.

DOI: 10.1103/PhysRevB.110.094412

I. INTRODUCTION

With the discovery of high-temperature superconductivity in cuprates by Bednorz and Müller [1] in 1986, enormous efforts have been underway to find superconductivity in other transition-metal-based oxide systems. In this regard, the most obvious place to look is the nickel-based transition-metal oxides or nickelates [2], isostructural and isoelectronic to the high-T_c cuprates. Almost three decades ago, Anisimov *et al.* [3] theoretically predicted that if Ni^{1+} ($S = 1/2$) is forced into square-planar coordination, an antiferromagnetic and insulating ground state should result, which can be further hole-doped to realize superconductivity in analogy with the high-T_c cuprates. The recent discovery of superconductivity in the thin films of hole-doped $NdNiO_2$ [4,5], $LaNiO_2$ [6,7], and $PrNiO_2$ [8,9] rekindled the interest in nickelates superconductors. The compounds RNiO$_2$ are the $n = \infty$ members of a much broader infinite-layer nickelate family with the general formula of $R_{n+1}Ni_nO_{2n+2}$, where R is either an alkaline-earth or a rare-earth ion, and n can take values $1, 2, 3, \ldots, \infty$. These infinite-layer nickelates can be variously located on the cuprate phase diagram depending on the Ni d electron count, granting access to various correlated ground states previously reported for the cuprates [2,10–12]. The validity of this phenomenology is only further reinforced with the discovery of superconductivity in thin films of "quintuple-layer" compound $Nd_6Ni_5O_{12}$ ($n = 5$) [13], which falls in the optimally doped region of the cuprate phase diagram [14].

In this work, we focus our attention on the $n = 3$ members, $R_4Ni_3O_8$ (R = La, Pr, and Nd). They crystallize in a tetragonal structure (space group $I4/mmm$) consisting of blocks of RNiO$_2$-type layers stacked along the c-axis, separated by intervening fluorite layers (RO_2) as shown in Fig. 1 (right panel). Each RNiO$_2$-type block is characterized by the presence of three parallel, infinitely extended NiO_2 layers, running along the ab-plane. The $R_4Ni_3O_8$ compounds are mixed-valent, containing Ni^{1+}/Ni^{2+} in the ratio of 2:1, which resembles the $3d^9/3d^8$ electronic configuration of Cu^{2+}/Cu^{3+} in high-T_c cuprates. The average Ni valence in $R_4Ni_3O_8$ is +1.33, i.e., a d filling value of 8.67, lying in the overdoped, Fermi liquid regime [11]. This, and their other similarities with cuprates, including a large orbital polarization of the unoccupied e_g states [11], strong Ni $3d$ and O $2p$ hybridization [15], and the square-planar arrangement of Ni, are reasons enough to investigate their physical properties at low temperatures.

$La_4Ni_3O_8$, $Pr_4Ni_3O_8$, and $Nd_4Ni_3O_8$ exhibit contrasting ground-state properties $La_4Ni_3O_8$ is a charge/spin (CS) stripe-ordered insulator, featuring a sharp semiconductor-to-insulator transition (loosely referred to as a metal-to-insulator or MIT transition) occurring concomitantly with the onset of charge/spin-stripe ordering at $T_N^* = 105$ K [16–20]. On the other hand, $Pr_4Ni_3O_8$ and $Nd_4Ni_3O_8$ show a metallic behavior over the whole temperature range with no indications of charge-stripe or spin ordering [11,13,21,22]. Understanding

*Contact author: surjeet.singh@iiserpune.ac.in

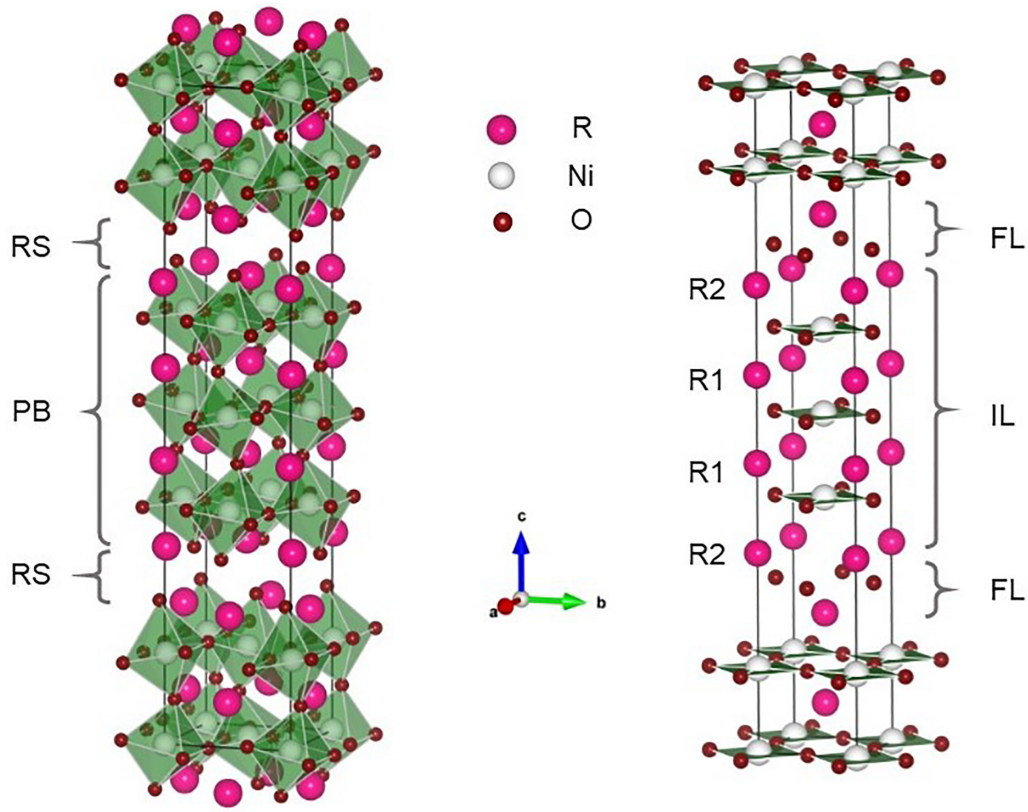

FIG. 1. The crystal structure of $R_4Ni_3O_{10}$ (left) and $R_4Ni_3O_8$ (right). RS and PB in the $R_4Ni_3O_{10}$ structure denote the rock salt layer (RS) and perovskite block (PB) stacked alternatively along the *c*-axis. Analogously, in the $R_4Ni_3O_8$ structure, FL and IL denote the stacked fluorite layer (FL) and infinite layered block (IL).

these stark differences in the ground-state properties as a function of *R*-site ionic radius, and a careful analysis of the magnetic properties of the *R*-sublattice in Pr and Nd analogs that was not well explored in the past, are important. However, these compounds require a part of Ni to be in an unfavorable +1 oxidation state, which makes their synthesis in pure phase somewhat challenging, hence limiting a detailed investigation of their physical properties.

In this study, we investigate the ground state of $La_4Ni_3O_8$, $Pr_4Ni_3O_8$, and $Nd_4Ni_3O_8$. At the same time, to understand the role of *R*-site ionic radius on the concomitant CS-stripe ordering in $La_4Ni_3O_8$, we investigate solid solutions of the form $(La_{1-x}R_x)_4Ni_3O_8$ (R = Pr, Nd). A phase diagram showing the evolution of T_N^* with an average *R*-site ionic radius, $r_{\bar{R}}$, has been constructed by combining data from the $(La_{1-x}Pr_x)_4Ni_3O_8$ and $(La_{1-x}Nd_x)_4Ni_3O_8$ series for various x. We show that T_N^* decreases nearly linearly upon decreasing $r_{\bar{R}}$ down to about $r_{\bar{R}} = 1.143$ Å beyond which it drops sharply to zero. Below r_c, the value of $r_{\bar{R}}$ at which T_N^* goes to zero, a new, weak anomaly in the specific heat emerges, whose onset temperature T^* increases linearly with decreasing $r_{\bar{R}}$. We therefore tentatively associate the sudden disappearance of charge/spin-stripe phase with the emergence of this new feature at T^* as $r_{\bar{R}}$ decreases below r_c.

The rest of the paper is organized as follows: The details of the experimental methods are given in Sec. II, followed by results and discussion in Sec. III. The details of sample synthesis, crystal structure, and low-temperature synchrotron x-ray diffraction, including the temperature variation of lattice parameters, appear in Secs. III A and III B. The electrical transport, magnetic susceptibility, and specific-heat data are discussed in Sec. III C. The summary and conclusions drawn are presented in Sec. IV.

II. EXPERIMENTAL METHODS

High-purity polycrystalline samples of the $n = 3$ member of the parent Ruddlesden Popper (RP) phases, i.e., $(La_{1-x}R_x)_4Ni_3O_{10}$ (R = Pr, Nd; $x = 0, 0.1, 0.5, 0.75, 0.9$, and 1.0), were prepared using the citrate method as described in [23]. The phase purity of these samples was confirmed using a Bruker D8 Advance powder x-ray diffractometer (PXRD). The corresponding trilayer T' nickelates were obtained by either the topotactic reduction using CaH_2 or reduction under a stream of H_2 gas (for obtaining $La_4Ni_3O_8$) or Ar/H_2 mixture (for obtaining Pr and Nd substituted samples). The chemical composition of the samples was analyzed using the energy-dispersive x-ray analysis (EDX) technique in a Zeiss Ultra Plus scanning electron microscope. To confirm the oxygen stoichiometry of our samples, we carried out the complete decomposition of the formed samples under 10% Ar-H_2 atmosphere, employing a heating rate of 10 K min^{-1} in a thermogravimetric analysis (TGA) setup (Netzsch STA 449 F1). High-resolution synchrotron powder x-ray diffraction experiments were carried out at the MSPD-BLO4 beamline of the ALBA synchrotron center, Barcelona, Spain. The

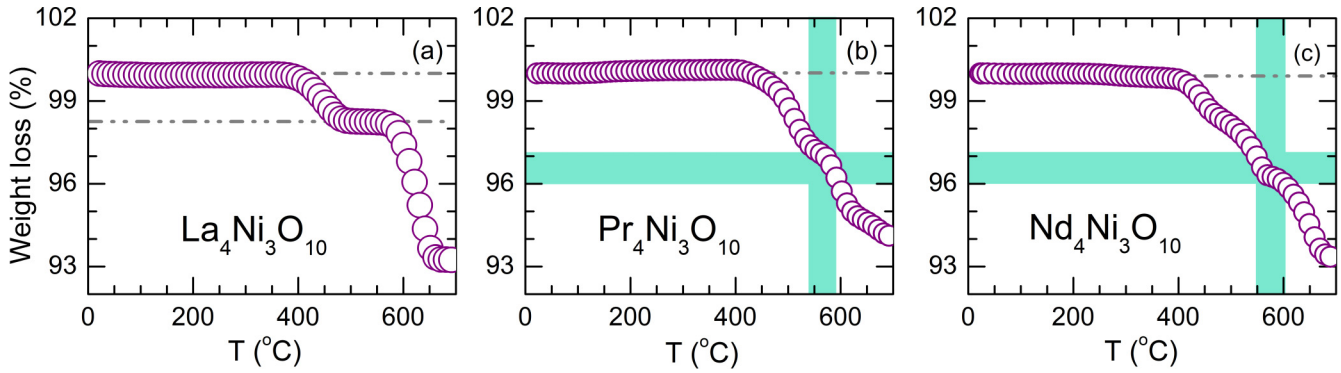

FIG. 2. Parts (a), (b), and (c) show the thermogravimetric analysis results of $La_4Ni_3O_{10}$, $Pr_4Ni_3O_{10}$, and $Nd_4Ni_3O_{10}$, respectively, carried out in Ar-H_2 (10%) atmosphere. The intersection of aqua-blue rectangular stripes in (b) and (c) mark the region where $R_4Ni_3O_8$ phase (R = Pr and Nd) can be stabilized. Part (a) shows that $La_4Ni_3O_8$ cannot be stabilized under Ar-H_2 (10%) flow (see text for details).

samples were prepared in the form of finely ground powders that were placed in a borosilicate capillary tube of 0.5 mm inner diameter. For cooling the sample down to 90 K, an Oxford Cryostream 700 series nitrogen blower was used, while for attaining temperatures lower than 90 K, He exchange gas was used. The diffractograms were collected in the range $0^\circ \leqslant 2\theta \leqslant 30^\circ$ using a step size of 0.003°. The incident beam energy was set at 38 keV ($\lambda = 0.3263$ Å) and a high-resolution detector (MAD26) was used to resolve any subtle structural modifications. On the other hand, the low-temperature laboratory-based PXRD measurements were performed on a Malvern Panalytical Empyrean Series 3 x-ray diffractometer with an Oxford Cryosystems PheniX closed-cycle helium cryostat, which can attain a lowest possible temperature of 12 K. The structural refinement was done by the Rietveld method using the FULLPROF suite [24].

Heat capacity, magnetization, and resistivity measurements were carried out using the Physical Property Measurement System (PPMS), Quantum Design, USA . The heat capacity of the sample holder and APIEZON N grease (addenda) was determined prior to measuring the sample. The magnetization measurements were carried out in the zero-field-cooled (ZFC) mode under an applied field of $H = 90$ kOe. Isothermal magnetization measurements were carried out at a temperature of 5 K up to an applied field of 90 kOe. For transport studies, bar-shaped specimens were cut from the sintered 4-3-10 pellets, which were reduced as described in the manuscript to obtain the corresponding 4-3-8 specimens. The resistivity and magnetoresistivity measurements were carried out using the four-probe method in the PPMS. The current $(I+, I-)$ and voltage $(V+, V-)$ contacts were made using a $\phi = 100\,\mu$m gold wire, glued to the sample using a conducting silver epoxy.

High-resolution transmission electron microscopy (HRTEM) was carried out using a JEOL JEM 2200FS 200 keV TEM instrument. The powder samples were finely ground in high-purity ethanol using an agate mortar and pestle to reduce the formation of agglomerates. Thereafter, less than a few mg of the ground powder was dispersed in an ethanol solution and subjected to sonication for a period of 30 min. A few droplets of the resultant suspension were drop-casted onto a TEM Cu grid using a micropipette. The Cu grid was then dried for 12 h in an evacuated desiccator, preheated at 60 °C in an oven for 15 min, and eventually loaded into the TEM sample chamber. Both HRTEM and SAED (selected area electron diffraction) patterns were collected for all the samples, and the analysis of the images was carried out using DIGITALMICROGRAPH (GMS-3) software package.

III. RESULTS AND DISCUSSION

A. Sample synthesis

As mentioned in the preceding section, the $R_4Ni_3O_8$ samples were prepared by reducing the parent RP or 4-3-10 phases. To obtain optimal conditions for the reduction, the 4-3-10 phase was first decomposed completely in a TGA setup under Ar-H_2 (10%) atmosphere as shown in Fig. 2. From these TGA plots, we conclude that $(Pr/Nd)_4Ni_3O_8$ samples and the $(La_{1-x}R_x)_4Ni_3O_8$ samples for $x > 0.5$ can be obtained by heating the sample at 360 °C for a duration ranging from 19 to 22 h. The reaction duration can be further reduced by increasing the temperature: e.g., 1.3 h at 500 °C ($Pr_4Ni_3O_8$), and ∼5 h at 470 °C ($Nd_4Ni_3O_8$). However, when reducing at higher temperatures, the gas flow had to be changed from Ar-H_2 (10%) to pure Ar, immediately at the end of the isotherm.

On the other hand, $La_4Ni_3O_8$ does not form under Ar-H_2 (10%) atmosphere as the step expected near 3.5% weight loss is missing in the TGA plot of Fig. 2(a). On the contrary, an unexpected step is present near 2% weight loss, which suggests the appearance of a new phase in accordance with the thermogravimetric data by Laccore *et al.* [25]. The synthesis of $La_4Ni_3O_8$ was therefore optimized under flowing ultrahigh-purity grade (UHP) H_2 gas. An isotherm temperature of 470 °C for 28 min with sample mass ranging from 40 to 50 mg was found ideal for obtaining pure $La_4Ni_3O_8$. A slight increment in the isotherm duration resulted in the decomposition of $La_4Ni_3O_8$ into La_2O_3 and Ni metal. And, decreasing the isotherm duration to 20–25 min, resulted in the formation of the 'new' phase alluded to above. (See Fig. S2 in the Supplemental Material [26]). Either this new phase corresponds to a different structure with stoichiometry $La_4Ni_3O_9$ [25], or it may be related to the $T^\dagger$ phase of $La_4Ni_3O_8$ reported by Cheng *et al.* [18]. Further characterizations are required to ascertain the exact crystal symmetry of this new phase. Alternatively, we also synthesized the $La_4Ni_3O_8$, and 10% (Pr/Nd) substituted $La_4Ni_3O_8$ samples, using the method of

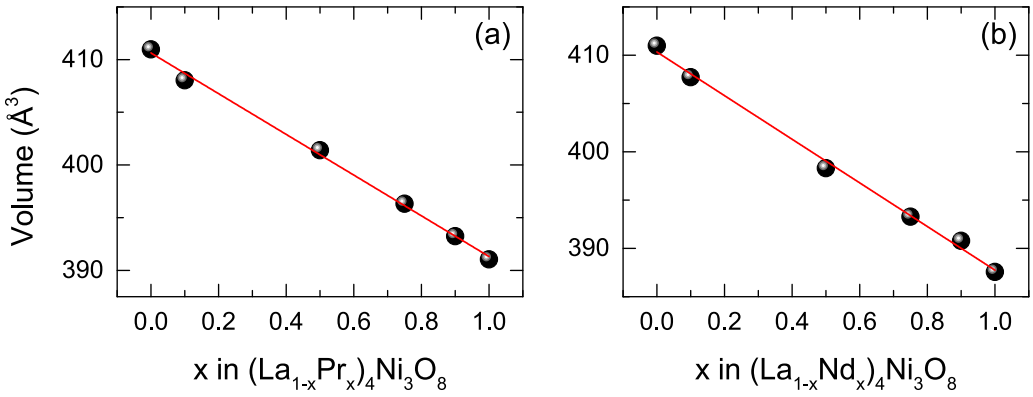

FIG. 3. Parts (a) and (b) show the variation of unit cell volume of $La_{1-x}Pr_xNi_3O_8$ and $La_{1-x}Nd_xNi_3O_8$ ($x = 0$, 0.1, 0.5, 0.75, 0.9, and 1.0) samples, respectively. The solid red line denotes a linear fit to the data.

topotactic reduction employing CaH_2 as a reducing agent. In this case, a sintered bar shaped sample of the parent RP or 4-3-10 phase was covered in an optimized amount of CaH_2 powder in a quartz ampoule in an argon-filled glove box. The quartz ampoule was then flame-sealed under vacuum (10^{-5} Torr) and subjected to heating at 360 °C for 36 h.

B. Structural characterization

The room-temperature crystal structure of $R_4Ni_3O_8$ (R = La, Pr, and Nd) compounds is shown in Fig. 1 (right panel). The powder diffraction patterns along with the Rietveld refinement for a few representative samples are shown in the Supplemental Material as Figs. S2 and S3 [26]. The variation of the unit cell volume with Pr or Nd mole fraction x in $(La_{1-x}Pr_x)_4Ni_3O_8$ and $(La_{1-x}Nd_x)_4Ni_3O_8$ samples is shown in Figs. 3(a) and 3(b), respectively. In both cases, a monotonic decrease of the cell volume with increasing x suggests that the smaller sized Pr/Nd successfully substitutes La in the structure, resulting in the formation of a homogenous solid-solution [27]. During the reduction from $R_4Ni_3O_{10}$ to $R_4Ni_3O_8$, the apical oxygen atoms are removed from the NiO_6 octahedra in the perovskite slab of the 4-3-10 structure. Thus, the octahedral arrangement around Ni in the parent RP phase modifies to a square-planar arrangement in the T' phase, transforming the perovskite trilayer block into an infinite-trilayer block comprising a stack of three infinitely extended planar NiO_2 layers. Henceforth, we shall refer to this block as a planar trilayer or infinite trilayer or quite simply as a trilayer block when there is no ambiguity. Similarly, upon reduction, the original rocksalt layer of the RP structure transforms into a fluorite-type RO_2 layer that acts as a buffer between successive trilayer blocks. The T' structure has two distinct rare-earth sites denoted by $R1$ and $R2$, where $R1$ lies in the trilayer block and $R2$ faces the fluorite layer on one side and the trilayer block on the other. Likewise, there are two distinct crystallographic sites for the Ni atoms denoted by Ni1 and Ni2, where Ni1 lies in the middle layer of the trilayer block and Ni2 in the outer layers facing the fluorite layer.

Figure 4 shows the temperature variation of lattice parameters of the parent $R_4Ni_3O_8$ (R = La, Pr, and Nd) samples down to 10 K. The temperature variation of the lattice parameters a and c of $La_4Ni_3O_8$ is shown in Fig. 4(a1). The corresponding plots showing the temperature variations of c/a and dV/dT, where V is the unit-cell volume, are shown Figs. 4(a2) and 4(a3), respectively. The lattice parameters exhibit a clear anomaly at $T \sim 105$ K, which coincides with the temperature T_N^* where the MIT or CS-stripe order is expected to set in on the basis of previous studies. Below T_N^*, the parameter a shows an anomalous increase with decreasing temperature; the parameter c, on the other hand, shows a steplike decrease; and accordingly, the ratio c/a presents a sharp, steplike decrease at T_N^*. These variations are in agreement with previous reports [11,18]. Contrary to $La_4Ni_3O_8$, the lattice parameters in $Pr_4Ni_3O_8$ [Fig. 4(b)] and $Nd_4Ni_3O_8$ [Fig. 4(c)] show a smooth and monotonic decrease upon cooling down to the lowest measured temperature of 10 K.

We come now to the temperature variation of lattice parameters of the Pr- or Nd-substituted samples. The lattice parameters of $La_2Pr_2Ni_3O_8$ and $La_2Nd_2Ni_3O_8$ are shown in Fig. 5. In $La_2Pr_2Ni_3O_8$, the 105 K anomaly suppresses down to a temperature of 55 K. The qualitative behavior of a and c across this transition remains similar to that described above for $La_4Ni_3O_8$, but the anomaly at T_N^* has weakened considerably, as shown in Fig. 5(a). However, in $La_2Nd_2Ni_3O_8$, T_N^* suppresses completely, with the lattice parameters showing a monotonically decreasing behavior down to the lowest temperature in our measurement, as shown in the right panels of Fig. 5, where the temperature variations of a, c, c/a, and V are shown. This difference (i.e., $La_2Pr_2Ni_3O_8$ showing a transition but $La_2Nd_2Ni_3O_8$ not) can be attributed to the ionic radii difference ($r_{Pr} > r_{Nd}$). The smaller size of Nd induces a larger negative chemical pressure compared to the same amount of Pr, and because the decreasing average R-site radius ($r_{\bar{R}}$) reduces T_N^*, it is expected that below a certain critical averaged R-site radius of $r_{\bar{R}} = r_c$ the transition will disappear. In other words, as $r_{\bar{R}} \to r_c$ from above ($r_{\bar{R}} > r_c$), $T_N^* \to 0$. The value of r_c has been recently shown to lie in the range $1.136 \leqslant r_{\bar{R}} \leqslant 1.140$ Å [28]. The average ionic radius of $R = La_{0.5}Nd_{0.5}$ ($r_{\bar{R}} = 1.1345$ Å) is clearly on the lower side of this range, whereas for $R = La_{0.5}Pr_{0.5}$ ($r_{\bar{R}} = 1.143$ Å), the average ionic radius is clearly on the higher side of this range and hence T_N^* is nonzero for this sample.

The temperature-dependent XRD data for the 10% Pr and Nd samples, collected using a laboratory-based diffractometer, are shown in Fig. S5 of the Supplemental Material [26]. The T_N^* suppresses to 99 and 92 K for Pr- and Nd-substituted samples, respectively.

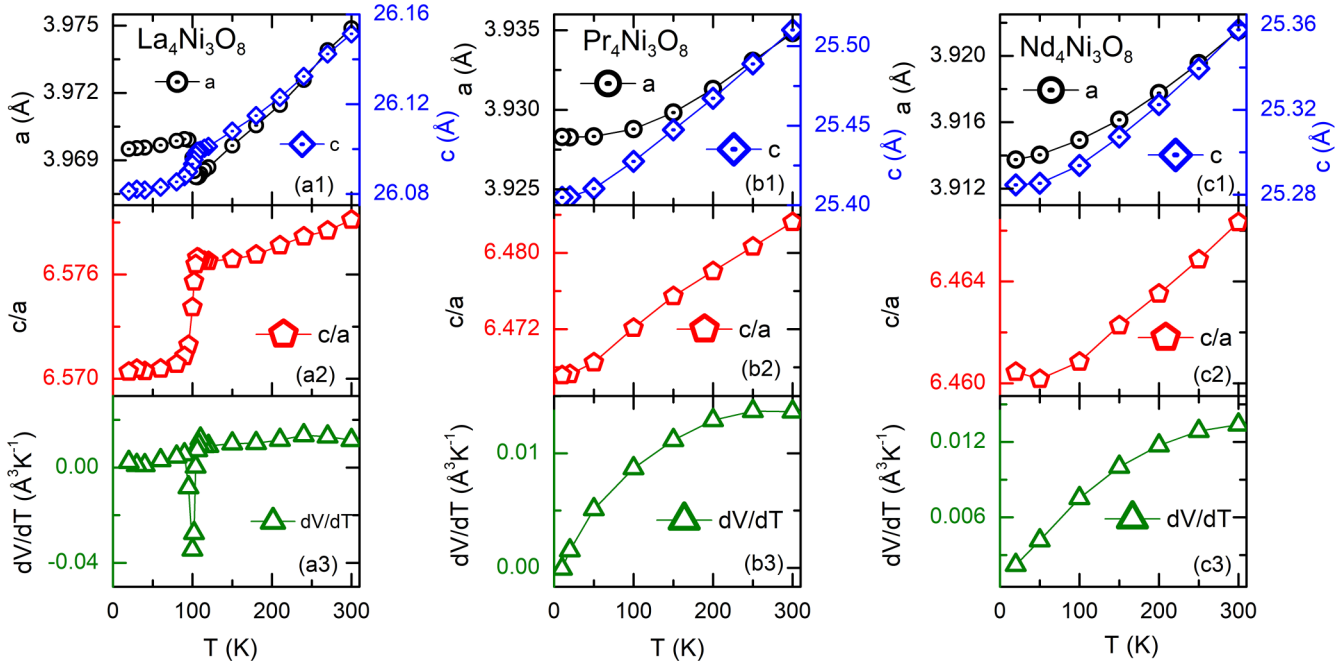

FIG. 4. The temperature variation of lattice parameters a and c (row 1: panels a1, b1, and c1), c/a ratio (row 2: panels a2, b2, and c2), and dV/dT (row 3: panels a3, b3, and c3) are shown for the $La_4Ni_3O_8$, $Pr_4Ni_3O_8$, and $Nd_4Ni_3O_8$ samples, respectively.

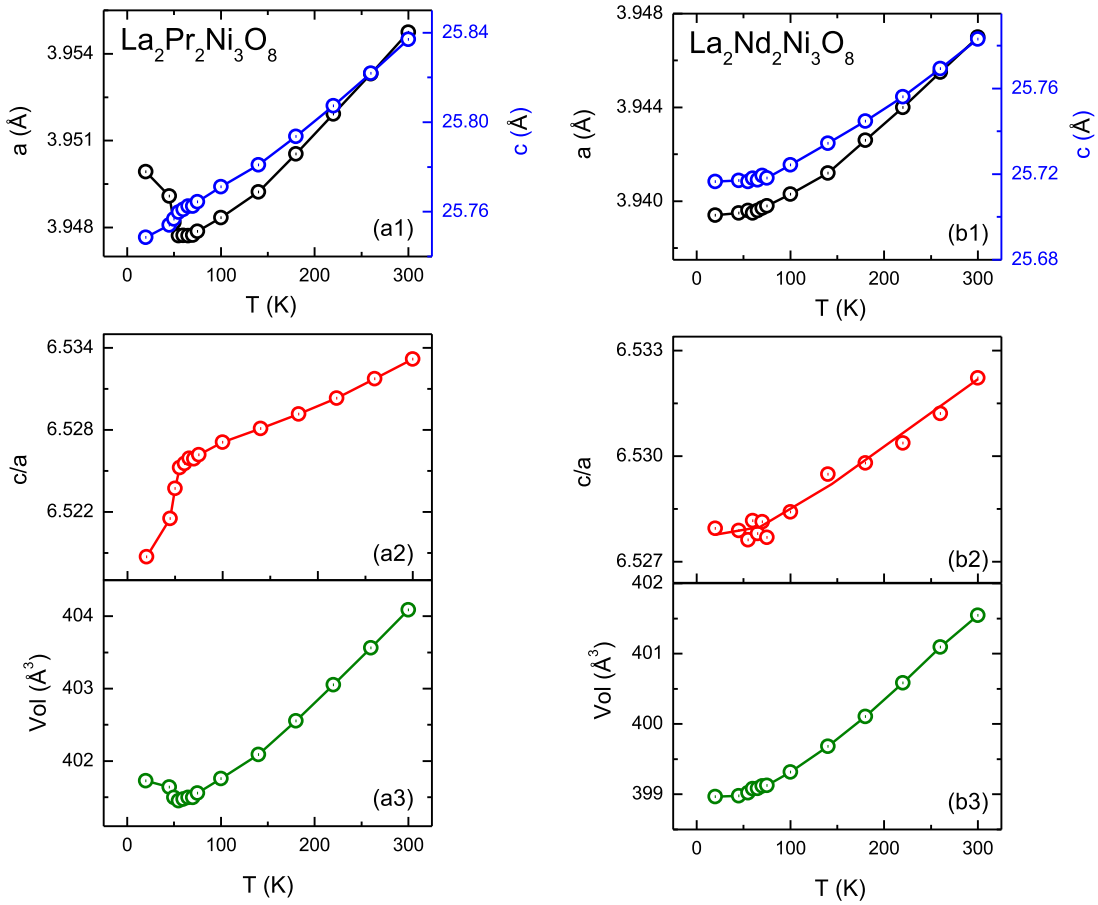

FIG. 5. Parts (a1)–(a3) and (b1)–(b3) show the temperature variation of lattice parameters, the c/a ratio, and the unit-cell volume for the $La_2Pr_2Ni_3O_8$ and $La_2Nd_2Ni_3O_8$ sample, respectively, measured from room temperature down to the lowest attainable temperature of 10 K.

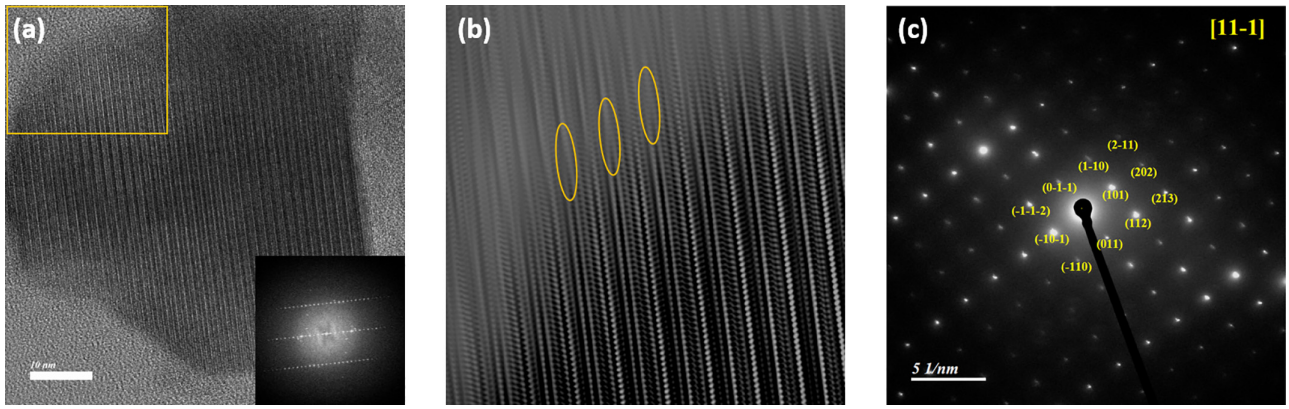

FIG. 6. (a) HRTEM micrograph of $Pr_4Ni_3O_8$; inset at the right bottom shows the FFT image of the micrograph. (b) IFFT of the region inside the yellow box shown in (a). The ellipses highlight the presence of stacking faults in the sample; (c) shows the SAED pattern taken on a highly crystalline region of the specimen, along the [1 1 − 1] zone axis with the *hkl* indices marked in yellow.

Figure 6(a) shows the HRTEM micrograph of our $Pr_4Ni_3O_8$ sample. The sample shows nicely lined up crystal planes with few defects in the form of stacking faults, some of which are highlighted in Fig. 6(b), where the fast Fourier transform (FFT) image of the bordered region in Fig. 6(a) is shown. No sign of intergrowth due to lower and higher n members, which typically plagues the sample quality, could be seen in our samples. The SAED pattern, shown in Fig. 6(c), consists of sharp spots indicative of a high crystallinity of the sample. The SAED pattern satisfies the reflection conditions expected for the $I4/mmm$ space group, in agreement with the previous HRTEM studies on $Nd_4Ni_3O_8$ [29].

C. Physical characterization

1. Magnetization

Figures 7(a) and 7(b) show the magnetic susceptibility, $\chi = M/H$, as a function of temperature for the $(La_{1-x}Pr_x)_4Ni_3O_8$ and $(La_{1-x}Nd_x)_4Ni_3O_8$ samples, respectively, where H is the applied field and M is the magnetization. In $La_4Ni_3O_8$ ($x = 0$), the concomitant charge/spin-stripe ordering is seen as a kink in the $\chi(T)$ plot near $T_N^* = 105$ K. A zoomed-in view of this feature is shown in the inset in Fig. 7(a), where it can be seen more clearly. The temperature at which this anomaly appears is in good agreement with the previous reports [16–18]. Upon substituting for La with Pr or Nd, the transition is suppressed. However, an important difference between the two substituents is that at low temperatures, the magnetization of the Nd series is significantly high compared to the Pr series for any given x. For example, for $Pr_4Ni_3O_8$, M/H at $T = 5$ K is about $\approx 6 \times 10^{-2}$ emu mol^{-1} Oe^{-1}, whereas in $Nd_4Ni_3O_8$, it is $\approx 26 \times 10^{-2}$ emu mol^{-1} Oe^{-1}; i.e., about four to five times that of $Pr_4Ni_3O_8$. Since the calculated effective moment on a free Pr^{3+} ion is comparable to that of Nd^{3+} (3.58 μ_B and 3.62 μ_B, respectively), the reduced low temperature magnetization of $Pr_4Ni_3O_8$ (and Pr substituted samples) suggests that the magnetic moment of Pr^{3+} in the crystal field split lowest J-multiplet ($J = 4$) is very small. Previously, we observed a similarly reduced low temperature magnetization in $Pr_4Ni_3O_{10}$ as compared to $Nd_4Ni_3O_{10}$ due to the nonmagnetic-singlet ground state associated with one of the two crystallographically inequivalent Pr ions in $Pr_4Ni_3O_{10}$ [23].

As a result, in $(La_{1-x}Pr_x)_4Ni_3O_8$ series, the magnetization signal originating from the Ni sublattice is not as heavily masked by the paramagnetic background of the rare-earth moments as in the Nd case. Thus, in the Pr-substituted series, the anomaly associated with CS-stripe ordering remains clearly discernible up to $x = 0.5$, and the value of T_N^* (indicated by arrows) is in fairly good accord with the temperature-dependent PXRD data discussed in the previous section, and also with the transition temperature reported for the $(La_{1-x}Pr_x)_4Ni_3O_8$ series in Ref. [28]. Beyond $x = 0.5$ (i.e., $x = 0.75$, 0.9, and 1), we observed a weak hump around 35 K. In Fig. S9 in the Supplemental Material [26], the derivative plots clearly capture the presence of this feature. It should be noted that this feature is present even in $Pr_4Ni_3O_8$ sample (in fact, it is relatively less dominant in $x = 0.75$ and 0.9). Since the size of this anomaly scales with Pr concentration, it is fair to conclude that it originates from the Pr sublattice and is likely a manifestation of the crystal-field splitting of the lowest J-multiplet of the Pr^{3+} ions.

Being a Kramers' ion with f^3 configuration (odd number of f electrons), the crystal-field-split ground state of Nd^{3+} ($J = 9/2$) will be either a doublet or a quartet as the Kramers' theorem forbids a singlet ground state. Hence, at low temperatures, both the Nd sites will contribute to the magnetization, and their paramagnetic background masks the CS-stripe anomaly associated with the Ni sublattice. This turned out to be true even for the sample with as small as 10% Nd substitution ($x = 0.1$). For higher value of x, the Curie-like behavior dominates over the whole temperature range.

2. Curie-Weiss analysis

For the $Pr_4Ni_3O_8$ and $Nd_4Ni_3O_8$ samples, χ^{-1} versus T plots look fairly linear with small curvatures above about 150 K. We therefore fitted the high-temperature data using the modified Curie-Weiss (CW) expression: $\chi = \chi_0 + C/(T - \theta_p)$, where C is the Curie constant from which the value of the effective magnetic moment (μ_{eff}) per formula unit can be obtained using $\mu_{eff} = \sqrt{8C}$, θ_p is the

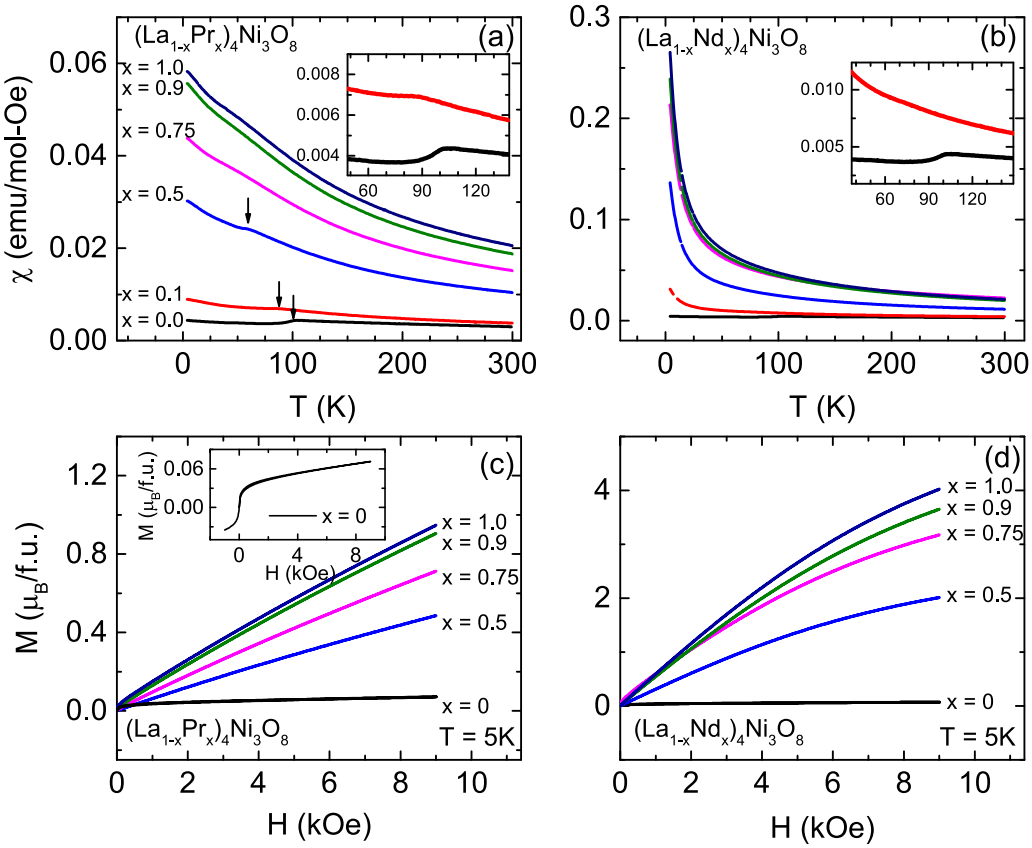

FIG. 7. Parts (a) and (b) show the zero-field-cooled magnetic susceptibility as a function of temperature for the $La_{1-x}Pr_xNi_3O_8$ and $La_{1-x}Nd_xNi_3O_8$ ($x = 0$, 0.1, 0.5, 0.75, 0.9, and 1.0) samples, respectively, measured under an applied field of 90 kOe; (c) and (d) show the isothermal magnetization at $T = 5$ K for the Pr and Nd series, respectively, measured from 0 to 90 kOe.

Weiss temperature, and χ_0 is the temperature-independent contribution arising from the core diamagnetism and the paramagnetism of Van Vleck or Pauli type. Treating χ_0, C, and θ_p as the fitting parameters, the best fit over the temperature range 150–300 K using the modified Curie-Weiss equation led to the following values of the fitting parameters: For $Pr_4Ni_3O_8$, $\chi_0 = 2.0 \times 10^{-3}$ emu mol^{-1} Oe^{-1}, $C =$ 7.3 emu mol^{-1} Oe^{-1} K, and $\theta_p = -96$ K. The corresponding values for $Nd_4Ni_3O_8$ are $\chi_0 = 1.6 \times 10^{-3}$ emu mol^{-1} Oe^{-1}, $C = 6.8$ emu mol^{-1} Oe^{-1} K, and $\theta_p = -49$ K. If we ignore the contribution of the Ni sublattice for the time being, then we get $\mu_{eff}/R^{3+} = 3.82\,\mu_B$ in $Pr_4Ni_3O_8$, and $3.69\,\mu_B$ in $Nd_4Ni_3O_8$, which exceeds the Hund's derived *free-ion* values, particularly in the Pr case. This suggests that the magnetization associated with the Ni sublattice should be non-negligible. Indeed, we know that the ratio Ni^{1+}/Ni^{2+} in T' structure is 2:1, and Ni^{1+} is in spin 1/2 state while Ni^{2+} can take two possible spin states: spin 0 (low-spin or LS) or spin 1 (high-spin or HS). Accordingly, the value of the quantity $3(\mu_{Ni})^2$ can be $14\,\mu_B^2$ (HS) or $6\,\mu_B^2$ (LS) (assuming the g factor to be 2 in each case). However, for any of these theoretical values to hold true, the d electrons of Ni should be localized. But since both $Pr_4Ni_3O_8$ and $Nd_4Ni_3O_8$ exhibit a metallic behavior, the d-electrons are partially localized with a reduced moment on Ni. A rough estimate of μ_{Ni}^2 using the relation $4(\mu_R)^2 + 3(\mu_{Ni})^2 = 8C$, by taking $\mu_R = 3.58$ (Pr) [3.62 (Nd)] μ_B and $C = 7.3$ (Pr) [6.8 (Nd)] emu mol^{-1} Oe^{-1}, suggests that the Ni^{2+} ions should be in their low-spin state, and the itinerant nature of Ni d-electrons increases upon going from La to Nd. The high values of θ_p and χ_0 in both cases are likely to have contribution from the large crystal-field splitting.

We, therefore, fitted the low-temperature data to extract the magnetic moment in the crystal-field-split ground-state, assuming it to be well isolated from the higher lying states at sufficiently low temperatures. In $Nd_4Ni_3O_8$, a satisfactory fit is obtained between 10 and 25 K, yielding: $\chi_0 = 0.031 \times 10^{-3}$ emu mol^{-1} Oe^{-1}, $C = 1.96$ emu mol^{-1} Oe^{-1} K, and $\theta_p = -4.7$ K. We see that the Curie constant, C, has reduced drastically from its high-temperature value suggesting that the magnetic moment per Nd ion in the crystal-field-split ground state is considerably smaller than the free-ion value. Interestingly, in the case of $Pr_4Ni_3O_8$, a satisfactory low-temperature Curie-Weiss fit could not be obtained despite adjusting the upper and lower temperature limits of the fitting range, indicating the complex nature of the magnetic ground state in $Pr_4Ni_3O_8$.

3. Isothermal magnetization

The isothermal magnetization at $T = 5$ K in both sets of substituted samples scales with the mole fraction of the rare-earth element present [Figs. 7(c) and 7(d)]. The temperature variation of $M(H)$ is quasilinear for $Pr_4Ni_3O_8$ and Pr-substituted samples, but a substantial nonlinearity can be

seen for the $Nd_4Ni_3O_8$ and Nd-substituted samples. In fact, in the Nd-substituted samples, the magnetization near the highest field is on the verge of plateauing. At $T = 5$ K, and under an applied magnetic field of 90 kOe, the magnetization of $Pr_4Ni_3O_8$ and $Nd_4Ni_3O_8$ is $\approx 1\mu_B$/f.u. and $\approx 4\,\mu_B$/f.u. Discarding the relatively small contribution of Ni, the experimental values of 1 and $4\,\mu_B$/f.u. are significantly smaller than the *free-ion* saturation magnetization of the constituent rare-earth ions, which is $g_J J = 12.8\ \mu_B$/f.u. ($Pr_4Ni_3O_8$) and 13.1 μ_B/f.u. ($Nd_4Ni_3O_8$), where g_J is the Landé g-factor. These reduced values can be attributed to the crystal-field effect, as at low temperatures only the low-lying crystal-field-split levels contribute to the magnetization. Between $Pr_4Ni_3O_8$ and $Nd_4Ni_3O_8$, the magnetization of $\approx 1\mu_B$/f.u. in $Pr_4Ni_3O_8$ is considerably smaller compared to $\approx 4\,\mu_B$/f.u. in $Nd_4Ni_3O_8$. This observation is in good agreement with the temperature dependent magnetization discussed above. Since this difference disappears at high temperatures where both Pr and Nd samples have comparable magnetization values, we conclude that the crystal field split ground state of Pr ions has a significantly smaller magnetic moment than that of the Nd ions. In fact, it is quite likely that either both or one of the two types of Pr ions in the unit cell has a non-magnetic ground state. This interpretation gains more weight if one notes that in the RP series (where the nonmagnetic singlet nature of one of the two Pr^{3+} ions in the structure has been shown), the magnitude of $M(H)$ between Nd and Pr samples has a similar relation [23].

In the inset of Fig. 7(c), the $M(H)$ for $La_4Ni_3O_8$ is shown, which is overshadowed in the main panel due to the R^{3+} sublattice. At 5 K, $M(H)$ of $La_4Ni_3O_8$ exhibits a ferromagnet-like steep initial increase, but at high fields $M(H)$ does not saturate but continues to increase linearly at a slower rate. This behavior is qualitatively similar to that previously reported [16]. However, the saturation moment of the ferromagnetic component (obtained by extrapolating the high-field linear part backwards to $H = 0$) is $\approx$ 0.01 μ_B/f.u. or $\approx$ 0.2 emu/g in our sample, but it is close to 0.75 emu/g in Ref. [16]. At the same time, dM/dH from the linear part is 2×10^{-3} emu mol^{-1} Oe^{-1} in both the studies. Zhang *et al.* [16] argued that these two components actually represent contributions from two different phases. While the saturation is due to the Ni-metal phase, which forms in trace amounts during the reduction process, the linear increase at high fields is intrinsic to the T' phase, which is well supported by the observation that dM/dH has the same value for the two independent samples, despite having very different saturation values. This suggests that the Ni-metal impurity is present in a smaller quantity in our sample. The Ni-metal impurity content in our sample, however, appears to be comparable to the polycrystalline samples in Ref. [17], where a similar value of saturation magnetization was observed.

Similarly, the $M(H)$ of $Pr_4Ni_3O_8$ samples in some previous studies is reported to exhibit a large ferromagnetic component [16,30]. In the supporting information provided with Ref. [16], the authors delved deeper into the intrinsic versus extrinsic origin of the ferromagnetic component, and they concluded that their data are difficult to reconcile with the intrinsic argument put forward in Ref. [30]. They observed that the ferromagnetic component is isotropic, unlike the quantity dM/dH, which exhibits a significant anisotropy between the in-plane and out-of-plane data, which led them to conclude with reasonable certainty that the ferromagnetic component has an extrinsic origin related to the presence of Ni metal, as discussed above. Zhang *et al.* also showed that the saturation magnetization of the ferromagnetic component is almost temperature-independent [11], which supports the presence of a ferromagnetic impurity in the form of Ni metal. This scenario is highly plausible since reduction beyond the optimized duration results in very rapid decomposition of the compound into R_2O_3 and Ni metal. In our $Pr_4Ni_3O_8$ (and Pr-substituted $La_4Ni_3O_8$ samples), the ferromagnetic component is either absent or too small to detect.

4. Specific heat

The molar specific heat (C_p) of the parent $R_4Ni_3O_8$ (R = La, Pr, and Nd) compounds is shown in Figs. 8(a)–8(c). In $La_4Ni_3O_8$, the concomitant charge/spin (CS)-stripe ordering is manifested as a peak near $T_N^* = 105$ K, as shown in Fig. 8(a). The temperature T_N^* of the anomaly is in excellent agreement with the previous reports [16–19], and with the position of the anomaly in the lattice parameters in Fig. 4(a1), 4(a2), and 4(a3), or with the position of the anomaly in the temperature variation of M/H for $x = 0$, as shown in Fig. 7(a).

Let us now turn to the specific heat of $Pr_4Ni_3O_8$ and $Nd_4Ni_3O_8$ samples, shown in Figs. 8(b) and 8(c), respectively. The first thing to note is that for both of these samples, the temperature variation of C_p is smooth over the entire temperature range. In particular, the 105 K anomaly present for the $La_4Ni_3O_8$ sample is absent for these samples, in line with the temperature-dependent PXRD and magnetization data, discussed earlier. Near room temperature, their specific heats are nearly equal, but about 20–25 J mol^{-1} K^{-1} higher than that of $La_4Ni_3O_8$. The excess specific heat is associated with the CF levels of the magnetic rare-earth ions.

While the high-temperature specific heat is featureless and varies smoothly, the low-temperature specific heat of Pr and Nd samples exhibits interesting features that are worth discussing here. We first note that the specific heat of $Pr_4Ni_3O_8$ near 20 K is approximately one-half that of $Nd_4Ni_3O_8$ at the same temperature. Furthermore, upon cooling below about 6 K, the specific heat of $Pr_4Ni_3O_8$ shows an anomalous behavior, which is more clearly depicted in the lower inset of Fig. 8(b), where C_p/T is plotted against T^2. We note that below temperature $T^* \approx 6$ K, C_p/T shows a sharp downturn, which does not show any magnetic field dependence.

On the other hand, the low-temperature specific heat of $Nd_4Ni_3O_8$ displays an upturn upon cooling below 5 K as shown in the upper inset of Fig. 8(c). Under an applied magnetic field, the onset temperature for this upturn shifts to higher values resulting in a broad peak at lower temperatures; this peak shifts to higher temperatures as the field strength increases—a feature typical of the Schottky-type anomaly, which, in this case, could be associated with the Zeeman split lowest crystal-field level of Nd^{3+} ions in $Nd_4Ni_3O_8$. In $Nd_4Ni_3O_{10}$, a similar behavior due to the Zeeman splitting of the Kramer's doublet ground state was previously reported [23]. Interestingly, when plotted as C_p/T versus T^2 [see the lower inset in Fig. 8(c)], the specific heat of $Nd_4Ni_3O_8$ also exhibits a sharp downturn, similar to that seen for $Pr_4Ni_3O_8$,

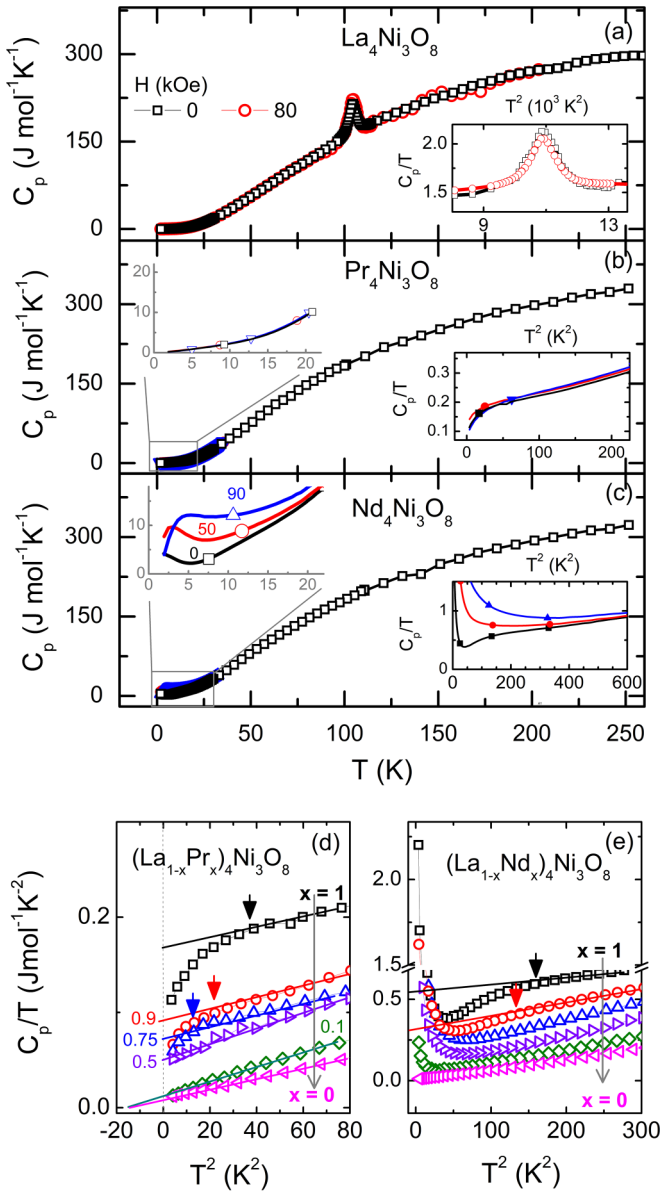

FIG. 8. Parts (a), (b), and (c) show the temperature variation of C_p for the $La_4Ni_3O_8$, $Pr_4Ni_3O_8$, and $Nd_4Ni_3O_8$ samples, respectively. The lower insets in panels (a), (b), and (c) show the C_p/T vs T^2 plots under various applied magnetic fields. In panels (b) and (c), the upper inset shows a zoomed-in view of the low-temperature specific heat. Note that the data points are dropped for clarity. The lines through the data points are a guide to the eye. Panels (d) and (e) show the zero-field C_p/T vs T^2 plot for the Pr and Nd series, respectively. The arrows pointing downward mark the position of T^* for various compositions using the same color as used for the corresponding plot. The legends used in (b) and (c) are the same.

below $T^* = 13$ K. Note that this feature is in addition to the upturn due to the Schottky effect.

The low-temperature specific heat of $(La_{1-x}R_x)_4Ni_3O_8$ (R = Pr, Nd) samples is shown in Figs. 8(d) and 8(e), respectively. In the Pr-substituted series, with decreasing Pr-content, the magnitude of C_p/T decreases progressively, and the temperature T^* also decreases to 5 K for $x = 0.9$ and 4 K for $x = 0.75$; however, for $x = 0.5$, C_p/T varies linearly without any perceptible downturn. Thus, T^* for this sample, if nonzero, lies below 2 K (the lowest temperature in our measurements). In the Nd series, the downturn in C_p/T, which was seen below 13 K in the pristine sample, shifts down to 11 K for $x = 0.9$. However, no such feature could be seen for $x = 0.75$ due to it proximity to the low-temperature upturn. If we plot T^* versus the average R-site lattice parameter, which is shown later in the manuscript (see Fig. 10), one sees a linear behavior as a function of $r_{\bar{R}}$ across the two series. This suggests that the anomaly T^* has a common origin in both $Pr_4Ni_3O_8$ and $Nd_4Ni_3O_8$, and it is controlled by the average R-site ionic radius. Going by this, T^* in $(La_{0.25}Nd_{0.75})_4Ni_3O_8$ ($x = 0.75$) should fall between 5 and 6 K. However, this coincides with the temperature below which the Schottky contribution dominates, masking the weak downturn for this sample.

We fitted the low temperature C_p for both the $Pr_4Ni_3O_8$ and $Nd_4Ni_3O_8$ using the expression $\frac{C_p}{T} = \gamma + \beta T^2$, where the coefficients γ and β represent the electronic and lattice contributions, respectively. For this purpose, we used the data above 6 K in the $Pr_4Ni_3O_8$ and 13 K in the $Nd_4Ni_3O_8$. Above these temperatures, the C_p/T versus T^2 plots look fairly linear over the temperature range shown in Figs. 8(d) and 8(e). The estimated γ value turned out to be 113 mJ mol^{-1} K^{-2} for $Pr_4Ni_3O_8$ and 485 mJ mol^{-1} K^{-2} for $Nd_4Ni_3O_8$. These values are unusually high, and one may be inclined to conclude that these samples exhibit a heavy-fermion behavior. However, before arriving at such a conclusion, one has to first carefully discard the crystal-field contribution arising from the low-lying crystal-field-split levels of R^{3+} ions. However, this is a complex task, requiring knowledge of the crystal-field-splitting scheme.

In the case of $La_4Ni_3O_8$, similar fitting was performed in the temperature range below 7 K, which resulted in $\gamma \approx 10$ mJ mol^{-1} K^{-2}, which is comparable to that for $La_4Ni_3O_{10}$ [23] that has a metallic ground state. Since the ground state of $La_4Ni_3O_8$ is insulating, its comparably large γ value might be arising from some excess specific heat associated with the long-range ordering of the Ni moments. Generally, this should have some power-law dependence, which should be properly fitted by extending the data to further lower temperatures where the lattice contribution becomes insignificant.

Before going further, we compare the low-temperature specific heat of $Pr_4Ni_3O_8$ and $Nd_4Ni_3O_8$ samples with their 4-3-10 analogs. We start by comparing the specific heat of the two Nd compounds, as in both of these compounds the crystal-field-split ground state of Nd is a Kramers doublet. Figure S7 in the Supplemental Material shows C_p versus T and C_p/T versus T^2 plots for the two Nd compounds [26]. In both cases, the sharp low-temperature upturn in C_p (or in C_p/T) is the precursory effect of the impending long-range ordering at temperatures below 2 K. This upturn is common to both samples and has the same interpretation. However, in $Nd_4Ni_3O_8$, there is an additional anomaly at T^*, which is more clearly revealed in the C_p/T versus T^2 plots. Note that this feature is not present in the $Nd_4Ni_3O_{10}$ sample, or more precisely, around $T^* = 13$ K no anomaly could be detected in the specific heat of $Nd_4Ni_3O_{10}$, which establishes that this feature is unique to the 4-3-8 phase.

In Fig. S8 in the Supplemental Material [26], we compare the specific heat of the two Pr compounds. As shown in

Fig. S8(a), C_p of $Pr_4Ni_3O_{10}$ exhibits a broad anomaly around 7 K. The magnetic entropy associated with this anomaly is estimated to be $2R\ln 2$ per formula unit in our previous paper [23], arising from the magnetic ordering of Pr^{3+} ions in the rocksalt layer (the two Pr ions in the perovskite block are shown to have a nonmagnetic singlet ground state). On the other hand, the specific heat of $Pr_4Ni_3O_8$ is not only significantly smaller compared to its 4-3-10 counterpart, it also does not show any peak, suggesting that all the Pr ions in $Pr_4Ni_3O_8$ are likely in their nonmagnetic singlet ground state. In the C_p/T versus T^2 plots shown in Fig. S8(b), the $Pr_4Ni_3O_8$ shows a similar anomaly at $T^* \approx 6$ K as seen for $Nd_4Ni_3O_8$. These differences once again indicate that the weak anomaly at T^* is a characteristic only of the 4-3-8 compounds and it is present for both Nd and Pr samples, and also varies systematically with x.

5. Electrical transport

The temperature-dependent normalized electrical resistivity $\rho/\rho_{300\,\mathrm{K}}$, where $\rho_{300\,\mathrm{K}}$ is the resistivity at 300 K, of the $(La_{1-x}Pr_x)_4Ni_3O_8$ and $(La_{1-x}Nd_x)_4Ni_3O_8$ samples, is shown in Figs. 9(a) and 9(b), respectively. The MIT associated with the CS-stripe ordering is clearly captured in $La_4Ni_3O_8$ near $T_N^* = 105$ K, in good agreement with previous reports [11,16–18]. Below this temperature, the resistivity shows a sharp increase upon cooling. In the $(La_{1-x}Pr_x)_4Ni_3O_8$ samples, the MIT is suppressed with the increase in the Pr substitution. The T_N^* in the Pr-substituted samples agrees fairly well with anomalies in the lattice parameter and magnetization data presented in the previous sections. In the Pr-rich samples, $x = 0.9$ and 0.75, the sharp increase in resistivity, characteristic of the MIT, is not seen, indicating that the critical doping required for the complete suppression of T_N^* lies in the range $0.5 \leqslant x \leqslant 0.75$, in agreement with Ref. [28]. Note that in Ref. [28], the chemical formula is written as $(Pr_{1-z}La_z)_4Ni_3O_8$, and T_N^* is shown to disappear between $0.6 \leqslant 1-z \leqslant 0.7$, which is contained within the interval found here. Although no MIT is seen for $x = 0.9$ and 0.75, the $\rho(T)$ exhibits a shallow minimum, with the slope $d\rho(T)/dT$ becoming steeper at very low temperatures. It should be pointed out that the resistivity of $Pr_4Ni_3O_8$ also show a similar resistivity upturn, ruling out any extrinsic origin or an origin related to sample inhomogeneity. This observation is consistent with several previous reports [11,13,21,22,31]. The metallic behavior of $Pr_4Ni_3O_8$ is in agreement with the theoretical calculations [12,32,33], where it was shown that the presence of a large hole pocket contribution from the Ni $d_{x^2-y^2}$ band at the Fermi level contributes to the charge transport. The residual resistivity ratio (RRR) for our metallic Pr-substituted samples (i.e., $0.75 \leqslant x \leqslant 1$) varies between 1 and 2. Such low values of RRR for these samples could be due to the presence of microcracks and stacking faults [see Fig. 6(b)], which may have appeared during the reduction process. Similar behavior is also seen for the La-Nd series, albeit with a difference: in this case, a clear MIT is seen only for $x = 0$ and 0.1. The upturn in the low-temperature resistivity of the Pr- or Nd-substituted metallic samples can arise due to a variety of reasons, including weak localization [34], electron-electron interaction, or the Kondo-like spin-dependent scattering mechanism [35]. To understand this, we tried fitting the low-temperature data to a logarithmic temperature dependence ($\ln T$) as well as to a $T^{0.5}$ dependence (see Fig. S11 in the Supplemental Material [26]). Both scenarios result in fits that do not look completely satisfactory, hence it is difficult to assign either of the two scenarios to explain the resistivity upturn.

The magnetoresistance (MR) refers to the change in resistance of a material under the influence of an applied magnetic field, and it is defined as MR (%) $= \{[\rho(H) - \rho(0)]/\rho(0)\} \times 100$, where H is the externally applied magnetic field; $\rho(H)$ and $\rho(0)$ represent resistivity (or resistance) of the sample in the presence and absence of a magnetic field, respectively. The MR data for the $Pr_4Ni_3O_8$ and $Nd_4Ni_3O_8$ samples are shown in Figs. 9(c) and 9(d), respectively. At 10 and 20 K, the MR of $Pr_4Ni_3O_8$ is positive over the whole temperature range. The field dependence is parabolic, except close to the origin, where the variation is linear. The quadratic dependence arises due to the extra scattering that the carriers encounter as they move under the influence of the Lorentz force. At lower temperatures of 5 and 2 K, the low-field MR is negative and it increases linearly up to 20–30 kOe, and thereafter shows a quadratic dependence, becoming positive at higher fields. The low-field linear region is a typical signature of the phenomenon known as weak antilocalization (WAL) [36–39]. The effect is overcome at high fields, restoring the quadratic behavior.

For the $Nd_4Ni_3O_8$ sample, a negative MR of nearly 4% has been observed at 2 K. The MR initially increases with the field before saturating at higher fields to a value close to 4% under a maximum applied field of ± 90 kOe. The magnitude of negative MR decreases as the temperature is raised from 2 to 5 K. However, it is positive over the whole range at 10 and 20 K. We believe that the negative MR at low temperatures is related to spin-disorder scattering [40]. Recall the presence of a Schottky anomaly in the low-temperature specific heat of $Nd_4Ni_3O_8$. This Schottky anomaly is due to the Zeeman splitting of the lowest crystal-field-split level. At low temperatures, as the magnetic field strength increases, more and more Nd ions occupy the lower Zeeman energy level; or, in other words, with increasing field strength more and more Nd moments line up along the field direction. This reduces the spin-disorder scattering, leading to a negative MR, as seen here. The MR saturates at high fields when the Nd moments are all more or less aligned along the field direction. An alternative possibility is that the negative MR in $Nd_4Ni_3O_8$ also arises due to the WAL effect as discussed above in the context of $Pr_4Ni_3O_8$. However, the saturation of MR at high magnetic fields makes this scenario less likely.

D. Phase diagram

Having analyzed the temperature dependence of powder x-ray diffraction data and various other physical quantities, we proceed to construct a tentative phase diagram depicting the variation of T_N^* (the concomitant charge/spin-stripe ordering and metal-to-insulator transition) and T^* (the low-temperature specific-heat anomaly) and the phases bounded by them. Table II in the Supplemental Material [26] summarizes the values of T_N^* and T^* for various values of $r_{\bar{R}}$ calculated as $r_R = (1-x)r_{\mathrm{La}} + xr_R$, where r_{La} and r_R are the ionic radii of La^{3+} and R^{3+} (R = Pr and Nd) in the eightfold coordination, and $\bar{R} \equiv La_{1-x}Pr_x$ or $La_{1-x}Nd_x$. The phase diagram is

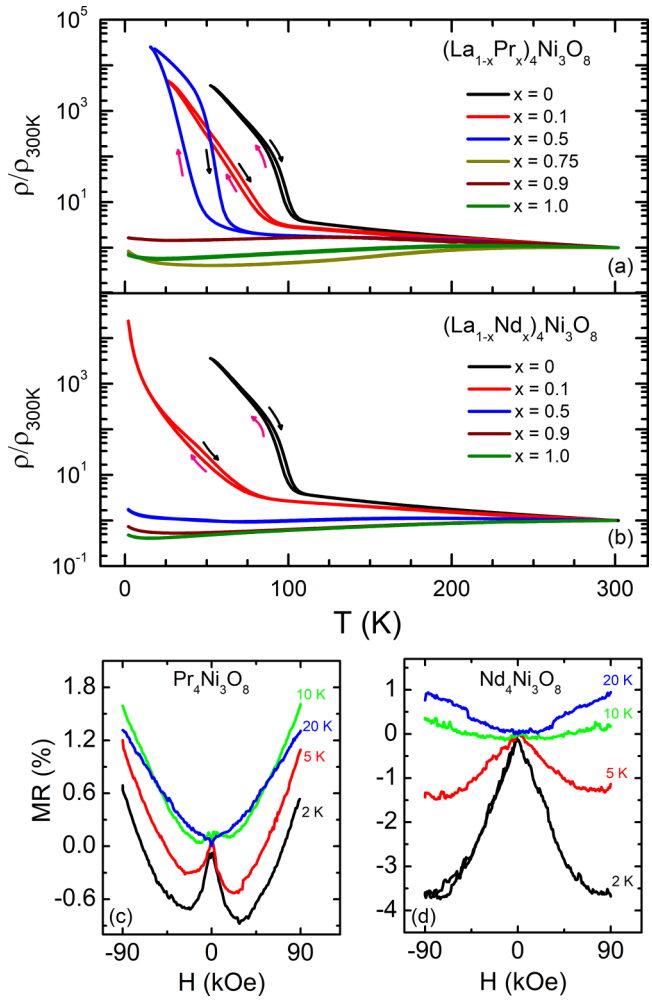

FIG. 9. Parts (a) and (b) show the value of $\rho(T)/\rho_{300\,\mathrm{K}}$ plotted as a function of temperature for $La_{1-x}Pr_xNi_3O_8$ and $La_{1-x}Nd_xNi_3O_8$ ($0 \leqslant x \leqslant 1.0$) samples, respectively. The arrows represent cooling and heating curves. Magnetoresistance of (c) $Pr_4Ni_3O_8$ and (d) $Nd_4Ni_3O_8$ at $T = 2$, 5, 10, and 20 K under an applied magnetic field ranging from -90 to 90 kOe.

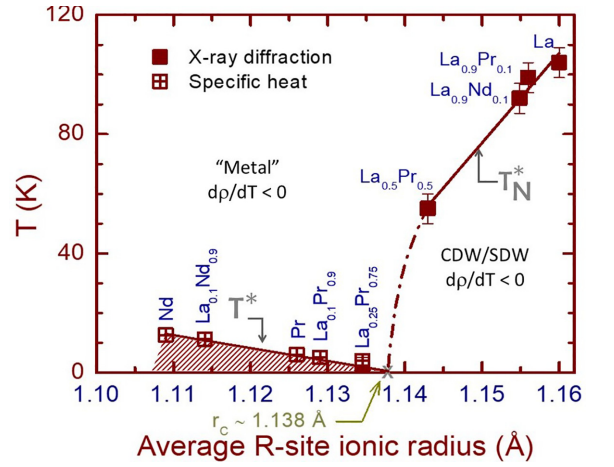

FIG. 10. A tentative phase diagram of $R_4Ni_3O_8$. The variation of T_N^* and T^* as a function of average R-site ionic radius ($r_{\bar{R}}$). r_c denotes the critical value of $r_{\bar{R}}$ around which T_N^* ($r_{\bar{R}} > r_c$) and T^* ($r_{\bar{R}} < r_c$) tends to zero. The phases are labeled as CDW/SDW for the charge/spin-stripe ordered phase where the temperature coefficient of resistivity $d\rho/dT < 0$, and "Metal" for the phase where $d\rho/dT > 0$. A weak resistivity upturn at low temperatures seen for all the samples has not been considered here. In the hashed region below T^*, the specific heat plotted as C_p/T shows a sharp decrease upon cooling. Other weaker crystal-field-originated anomalies above T^*, seen mainly in $d\chi/dT$, are not shown here.

shown in Fig. 10. With decreasing $r_{\bar{R}}$, the transition temperature T_N^* decreases almost linearly for both $(La_{1-x}Pr_x)_4Ni_3O_8$ and $(La_{1-x}Nd_x)_4Ni_3O_8$ down to $r_{\bar{R}} = 1.143$ Å, i.e., the composition $\bar{R} \equiv La_{0.5}Pr_{0.5}$. However, in the composition $\bar{R} \equiv La_{0.5}Nd_{0.5}$, which corresponds to $r_{\bar{R}} = 1.1345$ Å, T_N^* could not be detected either in x-ray diffraction or in its other physical properties. This suggests that T_N^* vanishes in the narrow range $1.134 < r_{\bar{R}} < 1.143$ Å. This agrees well with Ref. [28], where this range is even better defined as $1.136 < r_{\bar{R}} < 1.140$ Å. Thus, we can conclude that the T_N^* line drops quite suddenly to 0 once the amount of Pr or Nd substitution in $La_4Ni_3O_8$ exceeds critical values in this range corresponding to a critical R-site radius r_c.

The temperature T^* (the temperature below which C_P/T shows a sharp downturn) has been identified in this study and has no reference in the previous literature to the best of our knowledge. Since T^* has been observed for both $Pr_4Ni_3O_8$ and $Nd_4Ni_3O_8$ samples, and as this transition also scales almost linearly with $r_{\bar{R}}$, we believe that this is a characteristic temperature associated with the Ni d electrons, which depends on the R-site ionic radius but not on the exact identity or the f electron count of the concerned R ion *per se*. The variation of T^* with $r_{\bar{R}}$ is shown in the phase diagram in Fig. 10. In the limit $T^* \to 0$, the value of $r_{\bar{R}}$ at which T^* vanishes lies well within the range $1.136 < r_{\bar{R}} < 1.140$ Å. Hence, these two temperature scales (T_N^* and T^*) seem to be mutually exclusive; or, in other words, coming from the Nd or Pr side of the phase diagram ($r_{\bar{R}} > r_c$), one can argue that the electronic instability associated with the temperature scale T^* prevents the charge/spin-stripe ordering or MIT from setting in. The question of whether the disappearance of T^* with increasing $r_{\bar{R}}$ is related to the appearance of the charge/spin-stripe ordering in the region $r_{\bar{R}} > r_c$ can possibly be settled by performing further experiments to clarify the nature of the weak anomaly at T^*. The low-temperature neutron studies will also be useful in constructing a more complete phase diagram analogous to the phase diagram of manganites in Ref. [41], where the compositions around a critical value of the Mn-O-Mn bond angle, which is controlled by the R-site ionic radius, are shown to undergo a transition to an incommensurate lattice structure below the Néel temperature and subsequently to a commensurate phase upon further cooling. Similarly, in the pyrochlore iridates [42] and molybdates [43], the rare-earth ionic radii act as a tuning parameter to go from one correlated phase to another, typically involving metal-to-insulator transition.

IV. SUMMARY AND CONCLUSIONS

$La_4Ni_3O_8$ is an interesting system, showing concomitant charge/spin-stripe ordering and a metal-to-insulator transition near $T_N^* = 105$ K. Intriguingly, this transition does

not occur in its $Pr_4Ni_3O_8$ and $Nd_4Ni_3O_8$ analogs, both of which show a metallic behavior. Here, we examined the effect of progressively decreasing the *R*-site ionic radius by progressively substituting at the La site with Pr and Nd separately, leading to two sets of samples: $(La_{1-x}Pr_x)_4Ni_3O_8$ and $(La_{1-x}Nd_x)_4Ni_3O_8$, $0 \leqslant x \leqslant 1$. By combining the samples from the two doping series, we show that the transition temperature T_N^* initially decreases linearly as the average *R*-site ionic radius ($r_{\bar{R}}$) decreases, and then vanishes suddenly in the narrow range $1.134 \leqslant r_{\bar{R}} \leqslant 1.143$ Å, in agreement with Ref. [28], where this range is even better defined as $1.136 \leqslant r_{\bar{R}} \leqslant 1.140$ Å. A careful examination of the low-temperature specific heat revealed the presence of a weak anomaly, characterized by the temperature T^* below which C_P/T exhibits a sharp drop. Upon analyzing the variation of T^* with $r_{\bar{R}}$ for various intermediate compositions, including the end members $Pr_4Ni_3O_8$ ($T^* \sim 6$ K) and $Nd_4Ni_3O_8$ ($T^* \sim 13\,K$), we found that the T^* versus $r_{\bar{R}}$ plot follows a linearly decreasing trend with increasing $r_{\bar{R}}$, vanishing at $r_{\bar{R}} \approx 1.138$ Å, which lies exactly in the range where T_N^* disappears with decreasing $r_{\bar{R}}$. In other words, we demonstrate that the sudden disappearance of T_N^* upon decreasing $r_{\bar{R}}$ is associated with the emergence of a new phase in the region $r_{\bar{R}} < r_c$. The previous studies on these nickelates mainly focused on understanding the nature of the phase transition at T_N^* using advanced probes such as neutron scattering and angle-resolved photoemission spectroscopy. We propose that to gain a deeper understanding of the charge/spin-stripe ordering at (T_N^*) and its unusual dependence on the *R*-site ionic radius—particularly the sudden disappearance below a critical value ($r_{\bar{R}} = r_c$)—low-temperature experiments investigating the nature of the weak anomaly below (T^*) will be highly valuable. As T^* is controlled by $r_{\bar{R}}$, seen for both $Pr_4Ni_3O_8$ and $Nd_4Ni_3O_8$ (i.e., independent of the choice of the rare-earth), we argue that this transition does not originate from the rare-earth sublattice. Given the fact that Pr magnetism is weakened by the crystal-field splitting, the prospects of studying the nature of the anomaly at T^* are most favorable in $Pr_4Ni_3O_8$ and Pr-rich samples.

ACKNOWLEDGMENTS

S.S. acknowledges financial support from SERB (WMR/2016/003792). D.R. acknowledges financial support from IEEE Magnetics Society Educational Seed Funding. We are thankful to beamline scientists Francois Fauth, Catalin Popescu, and Aleksandr Missiul at the MSPD-BL04 beamline at ALBA Synchrotron facility. S.S. and D.R. would like to acknowledge the Department of Science and Technology, India (Grant No. SR/NM/Z-07/2015) for providing financial support for carrying out the synchrotron experiments at ALBA, and to the Jawaharlal Nehru Centre for Advanced Scientific Research (JNCASR) for facilitating it. S.S. and D.R. would like to thank UGC DAE Indore for providing the PPMS facility to carry out magnetotransport and magnetization experiments.

[1] J. G. Bednorz and K. A. Müller, Possible high T_c superconductivity in the Ba-La-Cu-O system, Z. Phys. B **64**, 189 (1986).
[2] J. F. Mitchell, A nickelate renaissance, Front. Phys. **9**, 813483 (2021).
[3] V. I. Anisimov, D. Bukhvalov, and T. M. Rice, Electronic structure of possible nickelate analogs to the cuprates, Phys. Rev. B **59**, 7901 (1999).
[4] D. Li, K. Lee, B. Y. Wang, M. Osada, S. Crossley, H. R. Lee, Y. Cui, Y. Hikita, and H. Y. Hwang, Superconductivity in an infinite-layer nickelate, Nature (London) **572**, 624 (2019).
[5] J. Fowlie, M. Hadjimichael, M. M. Martins, D. Li, M. Osada, B. Y. Wang, K. Lee, Y. Lee, Z. Salman, T. Prokscha, J.-M. Triscone, H. Y. Hwang, and A. Suter, Intrinsic magnetism in superconducting infinite-layer nickelates, Nat. Phys. **18**, 1043 (2022).
[6] S. Zeng, C. Li, L. E. Chow, Y. Cao, Z. Zhang, C. S. Tang, X. Yin, Z. S. Lim, J. Hu, P. Yang, and A. Ariando, Superconductivity in infinite-layer nickelate $La_{1-x}Ca_xNiO_2$ thin films, Sci. Adv. **8**, eabl9927 (2022).
[7] M. Osada, B. Y. Wang, B. H. Goodge, S. P. Harvey, K. Lee, D. Li, L. F. Kourkoutis, and H. Y. Hwang, Nickelate superconductivity without rare-earth magnetism: $(La, Sr)NiO_2$, Adv. Mater. **33**, 2104083 (2021).
[8] M. Osada, B. Y. Wang, B. H. Goodge, K. Lee, H. Yoon, K. Sakuma, D. Li, M. Miura, L. F. Kourkoutis, and H. Y. Hwang, A superconducting praseodymium nickelate with infinite layer structure, Nano Lett. **20**, 5735 (2020).
[9] M. Osada, B. Y. Wang, K. Lee, D. Li, and H. Y. Hwang, Phase diagram of infinite layer praseodymium nickelate $Pr_{1-x}Sr_xNiO_2$ thin films, Phys. Rev. Mater. **4**, 121801(R) (2020).
[10] A. S. Botana, V. Pardo, and M. R. Norman, Electron doped layered nickelates: Spanning the phase diagram of the cuprates, Phys. Rev. Mater. **1**, 021801(R) (2017).
[11] J. Zhang, A. S. Botana, J. W. Freeland, D. Phelan, H. Zheng, V. Pardo, M. R. Norman, and J. F. Mitchell, Large orbital polarization in a metallic square-planar nickelate, Nat. Phys. **13**, 864 (2017).
[12] A. S. Botana, K.-W. Lee, M. R. Norman, V. Pardo, and W. E. Pickett, Low valence nickelates: Launching the nickel age of superconductivity, Front. Phys. **9**, 813532 (2022).
[13] G. A. Pan, D. Ferenc Segedin, H. LaBollita, Q. Song, E. M. Nica, B. H. Goodge, A. T. Pierce, S. Doyle, S. Novakov, D. Córdova Carrizales, A. T. N'Diaye, P. Shafer, H. Paik, J. T. Heron, J. A. Mason, A. Yacoby, L. F. Kourkoutis, O. Erten, C. M. Brooks, A. S. Botana *et al.*, Superconductivity in a quintuple-layer square-planar nickelate, Nat. Mater. **21**, 160 (2022).
[14] B. Keimer, S. A. Kivelson, M. R. Norman, S. Uchida, and J. Zaanen, From quantum matter to high-temperature superconductivity in copper oxides, Nature (London) **518**, 179 (2015).
[15] J. Q. Lin, P. Villar Arribi, G. Fabbris, A. S. Botana, D. Meyers, H. Miao, Y. Shen, D. G. Mazzone, J. Feng, S. G. Chiuzbăian, A. Nag, A. C. Walters, M. García-Fernández, K.-J. Zhou, J. Pelliciari, I. Jarrige, J. W. Freeland, J. Zhang, J. F. Mitchell,

V. Bisogni *et al.*, Strong superexchange in a $d^{9-\delta}$ nickelate revealed by resonant inelastic x-ray scattering, Phys. Rev. Lett. **126**, 087001 (2021).

[16] J. Zhang, Y.-S. Chen, D. Phelan, H. Zheng, M. R. Norman, and J. F. Mitchell, Stacked charge stripes in the quasi-2D trilayer nickelate $La_4Ni_3O_8$, Proc. Natl. Acad. Sci. USA **113**, 8945 (2016).

[17] V. V. Poltavets, K. A. Lokshin, A. H. Nevidomskyy, M. Croft, T. A. Tyson, J. Hadermann, G. Van Tendeloo, T. Egami, G. Kotliar, N. ApRoberts-Warren, A. P. Dioguardi, N. J. Curro, and M. Greenblatt, Bulk magnetic order in a two-dimensional Ni^{1+}/Ni^{2+} (d^9/d^8) nickelate, isoelectronic with superconducting cuprates, Phys. Rev. Lett. **104**, 206403 (2010).

[18] J.-G. Cheng, J.-S. Zhou, J. B. Goodenough, H. D. Zhou, K. Matsubayashi, Y. Uwatoko, P. P. Kong, C. Q. Jin, W. G. Yang, and G. Y. Shen, Pressure effect on the structural transition and suppression of the high-spin state in the triple-layer T'−$La_4Ni_3\mathbf{O}_8$, Phys. Rev. Lett. **108**, 236403 (2012).

[19] J. Zhang, D. M. Pajerowski, A. S. Botana, H. Zheng, L. Harriger, J. Rodriguez-Rivera, J. P. C. Ruff, N. J. Schreiber, B. Wang, Y.-S. Chen, W. C. Chen, M. R. Norman, S. Rosenkranz, J. F. Mitchell, and D. Phelan, Spin stripe order in a square planar trilayer nickelate, Phys. Rev. Lett. **122**, 247201 (2019).

[20] N. ApRoberts-Warren, A. P. Dioguardi, V. V. Poltavets, M. Greenblatt, P. Klavins, and N. J. Curro, Critical spin dynamics in the antiferromagnet $la_4ni_3o_8$ from ^{139}La nuclear magnetic resonance, Phys. Rev. B **83**, 014402 (2011).

[21] T. Miyatake, Y. Wako, S. Tsukamoto, I. Umehara, and M. Uehara, Chemical doping to ni-sites in layered nickelate $Pr_4Ni_3O_8$ for high-tc superconductor candidate, Soc. Sci. Res. Netw. (2022), doi:10.2139/ssrn.4080321.

[22] A. Nakata, S. Yano, H. Yamamoto, S. Sakura, Y. Kimishima, and M. Uehara, The first observation of metallic behaviour in $Nd_{3.5}Sm_{0.5}Ni_3O_8$, Adv. Condens. Matter Phys. **2016**, 5808029 (2016).

[23] D. Rout, S. R. Mudi, M. Hoffmann, S. Spachmann, R. Klingeler, and S. Singh, Structural and physical properties of trilayer nickelates $R_4ni_3o_{10}$ (R = La, Pr, and Nd), Phys. Rev. B **102**, 195144 (2020).

[24] J. Rodríguez-Carvajal, Recent advances in magnetic structure determination by neutron powder diffraction, Phys. B **192**, 55 (1993).

[25] P. Lacorre, Passage from t-type to t'-type arrangement by reducing $Nd_{3.5}Sm_{0.5}Ni_3O_8$ (r = la, pr, nd), J. Solid State Chem. **97**, 495 (1992).

[26] See Supplemental Material at http://link.aps.org/supplemental/10.1103/PhysRevB.110.094412 for thermogravimetric data, Rietveld analysis, structural (x-ray diffraction) evolutions in going from 4-3-10 to 4-3-8 phase, high-temperature specific heat, and comparison of low-temperature specific heats of 4-3-10 and 4-3-8 compounds.

[27] R. D. Shannon, Revised effective ionic radii and systematic studies of interatomic distances in halides and chalcogenides, Acta Cryst. Sec. A **32**, 751 (1976).

[28] X. Chen, H. Zheng, D. P. Phelan, H. Zheng, S. H. Lapidus, M. J. Krogstad, R. Osborn, S. Rosenkranz, and J. F. Mitchell, Competing charge/spin-stripe and correlated metal phases in trilayer nickelates $(Pr_{1-x}Lax)_4Ni_3O_8$, Chem. Mater. **34**, 4560 (2022).

[29] R. Retoux, J. Rodriguez-Carvajal, and P. Lacorre, Neutron diffraction and tem studies of the crystal structure and defects of $Nd_4Ni_3O_8$, J. Solid State Chem. **140**, 307 (1998).

[30] S. Huangfu, Z. Guguchia, D. Cheptiakov, X. Zhang, H. Luetkens, D. J. Gawryluk, T. Shang, F. O. von Rohr, and A. Schilling, Short-range magnetic interactions and spin-glass behavior in the quasi-two-dimensional nickelate $Pr_4Ni_3o_8$, Phys. Rev. B **102**, 054423 (2020).

[31] K. Kobayashi, H. Yamamoto, A. Nakata, I. Umehara, M. Uehara, H. Yamamoto, A. Nakata, I. Umehara, and M. Uehara, Electrical resistivity measurements under high pressure for $Nd_{3.5}Sm_{0.5}Ni_3O_8$, JJAP Conf. Proc. **6**, 011106 (2017).

[32] E. M. Nica, J. Krishna, R. Yu, Q. Si, A. S. Botana, and O. Erten, Theoretical investigation of superconductivity in trilayer square-planar nickelates, Phys. Rev. B **102**, 020504(R) (2020).

[33] J. Karp, A. Hampel, M. Zingl, A. S. Botana, H. Park, M. R. Norman, and A. J. Millis, Comparative many-body study of $Pr_4Ni_3O_8$ and $ndnio_2$, Phys. Rev. B **102**, 245130 (2020).

[34] E. Abrahams, P. W. Anderson, D. C. Licciardello, and T. V. Ramakrishnan, Scaling theory of localization: Absence of quantum diffusion in two dimensions, Phys. Rev. Lett. **42**, 673 (1979).

[35] J. Kondo, Resistance Minimum in dilute magnetic alloys, Prog. Theor. Phys. **32**, 37 (1964).

[36] S. Hikami, A. I. Larkin, and Y. Nagaoka, Spin-orbit interaction and magnetoresistance in the two dimensional random system, Prog. Theor. Phys. **63**, 707 (1980).

[37] Y. Xing, Y. Sun, M. Singh, Y.-F. Zhao, M. H. W. Chan, and J. Wang, Electronic transport properties of topological insulator films and low dimensional superconductors, Front. Phys. **8**, 491 (2013).

[38] A. Laitinen, M. Kumar, and P. J. Hakonen, Weak antilocalization of composite fermions in graphene, Phys. Rev. B **97**, 075113 (2018).

[39] M. Jenderka, J. Barzola-Quiquia, Z. Zhang, H. Frenzel, M. Grundmann, and M. Lorenz, Mott variable-range hopping and weak antilocalization effect in heteroepitaxial Na_2IrO_3 thin films, Phys. Rev. B **88**, 045111 (2013).

[40] C. Haas, Spin-disorder scattering and magnetoresistance of magnetic semiconductors, Phys. Rev. **168**, 531 (1968).

[41] T. Goto, T. Kimura, G. Lawes, A. P. Ramirez, and Y. Tokura, Ferroelectricity and giant magnetocapacitance in perovskite rare-earth manganites, Phys. Rev. Lett. **92**, 257201 (2004).

[42] K. Ueda, H. Fukuda, R. Kaneko, J. Fujioka, and Y. Tokura, Evolution of possible weyl semimetal states across the mott transition in pyrochlore iridates induced by hole doping, Phys. Rev. B **102**, 245131 (2020).

[43] H. Ishikawa, S. Xu, Y. Moritomo, A. Nakamura, Y. Ohishi, and K. Kato, High-pressure structural investigation of ferromagnetic $Nd_2Mo_2O_7$, Phys. Rev. B **70**, 104103 (2004).